ELSEVIER

Nuclear Instruments and Methods in Physics Research A 460 (2001) 239–265

NUCLEAR INSTRUMENTS & METHODS IN PHYSICS RESEARCH Section A

www.elsevier.nl/locate/nima

The CLAS forward electromagnetic calorimeter

M. Amarian[a], G. Asryan[a], K. Beard[b], W. Brooks[c], V. Burkert[c], T. Carstens[c], A. Coleman[b], R. Demirchyan[a], Yu. Efremenko[d], H. Egiyan[a,1], K. Egiyan[a], H. Funsten[b], V. Gavrilov[d], K. Giovanetti[e], R.M. Marshall[f], B. Mecking[c], R.C. Minehart[f], H. Mkrtchan[a], M. Ohandjanyan[a], Yu. Sharabian[a], L.C. Smith[f,*], S. Stepanyan[a,2], W.A. Stephens[f], T.Y. Tung[b,3], C. Zorn[c]

[a]*YerPi, Yerevan, Armenia*
[b]*The College of William and Mary, Williamsburg, VA 23185, USA*
[c]*Thomas Jefferson National Accelerator Facility, Newport News, VA 23606, USA*
[d]*ITEP, Moscow, Russia*
[e]*James Madison University, Harrisonburg, VA, 22807, USA*
[f]*University of Virginia, Charlottesville, VA 22901, USA*

Received 23 February 2000; received in revised form 4 August 2000; accepted 12 August 2000

Abstract

The CEBAF Large Acceptance Spectrometer (CLAS) at Jefferson Lab utilizes six iron-free superconducting coils to provide an approximately toroidal magnetic field. The six sectors are instrumented individually to form six independent spectrometers. The forward region ($8^\circ < \theta < 45^\circ$) of each sector is equipped with a lead–scintillator electromagnetic sampling calorimeter (EC), 16 radiation lengths thick, using a novel triangular geometry with stereo readout. With its good energy and position resolution, the EC is used to provide the primary electron trigger for CLAS. It is also used to reject pions, reconstruct π° and η decays and detect neutrons. This paper treats the design, construction and performance of the calorimeter. © 2001 Elsevier Science B.V. All rights reserved.

PACS: 29.40.Vj

Keywords: CLAS; Calorimeter; Calibration; Scintillator

1. Overview

The Continuous Beam Electron Accelerator Facility (CEBAF) at Jefferson Lab provides up to 6 GeV electrons to three experimental halls. Hall B houses the CEBAF Large Acceptance Spectrometer (CLAS) [17], which is designed to study multi-particle final-state reactions induced by photons and electrons at luminosities up to $10^{34}\,\mathrm{cm}^{-2}\,\mathrm{s}^{-1}$.

* Correspondence address: Physics Department, University of Virginia, McCormick Rd., Charlottesville, VA 22901, USA. Tel.: +1-804-924-6806.

[1] Present address: The College of William and Mary, Williamsburg, VA 23185, USA.

[2] Present address: Christopher Newport University, Newport News, VA 23606, USA.

[3] Present address: Lucent Technologies, Holmdel, NJ 07733-3030, USA.

0168-9002/01/$ - see front matter © 2001 Elsevier Science B.V. All rights reserved.
PII: S0168-9002(00)00996-7

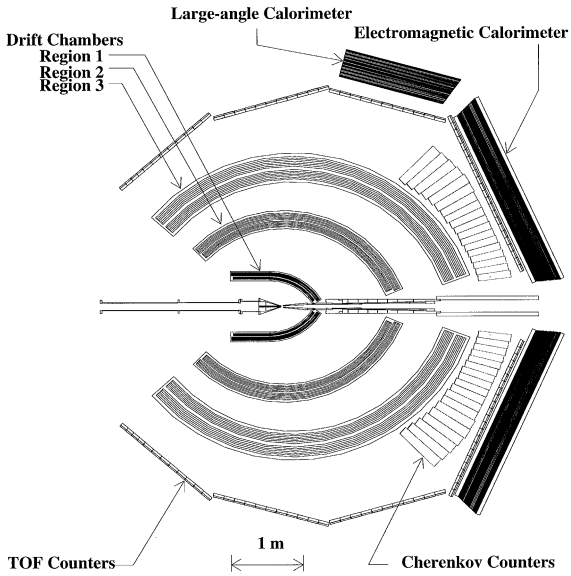

Fig. 1. Horizontal midplane slice through the CLAS detector. The beam enters from the left. Forward electromagnetic calorimeters and Cherenkov counters provide the hardware electron trigger.

A schematic view of the CLAS is shown in Fig. 1. Six superconducting coils generate a toroidal magnetic field having azimuthal symmetry. The coils divide CLAS into six sectors, each functioning as an independent magnetic spectrometer. Each sector is instrumented with multi-wire drift chambers (DC), time-of-flight scintillation counters (SC) and for the forward region ($8^\circ < \theta < 45^\circ$), a gas-filled threshold Cherenkov counter (CC) and an electromagnetic calorimeter (EC). The sensitive region of each sector covers a range of polar angles from 10° to 150°. Azimuthal coverage for CLAS is limited only by the magnet coils, and is approximately 90% at large angles and 50% at forward angles.

This paper describes the design, construction, calibration and initial performance of the calorimeter, which serves three main functions in CLAS:

- Detection and triggering of electrons at energies above 0.5 GeV. The total energy deposited in the EC is available at the trigger level to reject minimum ionizing particles or to select a particular range of scattered electron energy.
- Detection of photons at energies above 0.2 GeV, allowing π° and η reconstruction from the measurement of their 2γ decays.
- Detection of neutrons, with discrimination between photons and neutrons using time-of-flight measurements.

2. Requirements

The design of the calorimeter was based on the following criteria, the determination of which is discussed in the following sections:

- e/γ energy resolution $\sigma/E \leqslant 0.1/\sqrt{E\,(\mathrm{GeV})}$;
- position resolution $\delta r \approx 2$ cm at 1 GeV;
- π/e rejection greater than 99% at $E \leq 1$ GeV;
- fast (< 100 n) total energy sum for the event trigger;
- mass resolution for two photon decays $\delta m/m \leq 0.15$;
- neutron detection efficiency $> 50\%$ for $E_n > 0.5$ GeV;
- time-of-flight resolution ≈ 1 ns.

2.1. Electron identification and pion rejection

The transverse and longitudinal granularity requirements of the calorimeter were based on several factors. First, the measurement of cross-sections to an absolute accuracy of a few percent requires high electron detection efficiencies ($> 98\%$), and large hadron rejection factors ($\approx 10^2$), independent of energy, incident angle and impact position on the EC. Pion rejection is provided by the threshold CC for momenta less than 2.8 GeV/c, but at higher momenta identification of pions and electrons must be obtained by comparing the energy deposited in the EC with the momentum determined from the curvature of the trajectories in the magnetic field, and from differences in the pattern of energy deposition in the EC. Second, because of the large solid angle subtended by each EC module, enough segmentation to distinguish multiple hits within one sector is needed. Finally, good particle identification depends on matching EC hits with those in the SC and CC detectors as well as with drift chamber tracks projected onto the EC detector plane.

2.2. Fast analog sum of the energy

In many experiments, determination of the four-momentum transfer Q^2 and the total hadronic mass W is desirable at the trigger level. This requires a fast analog sum to determine the total energy deposited within an EC module, and also sets resolution requirements for other CLAS detector elements that are included in the trigger. For example, the SC angular resolution of approximately $\delta\theta \approx 3^\circ$ combined with the EC energy resolution of $\approx 10\%$ allows CLAS to be triggered over a relatively narrow W window at different values of Q^2.

2.3. Reconstruction of π° and η decays

For some experiments it is necessary to reconstruct π° and η mesons with momenta up to 3.5 GeV/c from their two photon decays. From the measured energy E_γ and polar angle θ_γ of each photon, the invariant mass $M_{2\gamma}$ is given by

$$M_{2\gamma} = 2E_{\gamma 1}E_{\gamma 2}(1 - \cos\ (\theta_{\gamma 1} + \theta_{\gamma 2})). \quad (1)$$

A mass resolution of $\delta m/m < 0.15$ is needed to provide adequate π°–η separation and to reject a background of pions. Eq. (1) shows that the particle mass resolution is determined by errors in the measurement of the energies and opening angle of the decay photons. Assuming an equal energy resolution for photons and electrons, an angular resolution of $\delta\theta \approx 10$ mrad is necessary to reconstruct π° events with the required mass resolution at the highest momenta. For η decays the mass resolution is totally dominated by the uncertainties in the decay photon energies.

2.4. Neutron detection

Good neutron detection efficiency is important for a number of experiments. Due to the large hadronic interaction length for neutrons, detection efficiencies exceeding 50% can be achieved without increasing the total radiation length beyond what is needed to contain electromagnetic (EM) showers. The only practical way to distinguish photons from neutrons for momenta up to 2.5 GeV/c is to use time of flight. A time resolution of $\sigma \approx 1$ ns is required to achieve this goal.

3. Design

After consideration of several schemes and the testing of small prototypes [1,2], a sampling calorimeter made of alternating layers of scintillator strips and lead sheets with a total thickness of 16 radiation lengths was chosen. A lead : scintillator thickness ratio of 0.2 was used, requiring 40 cm of scintillator and 8 cm of lead per module. With this ratio, approximately $\frac{1}{3}$ of the energy in a shower is deposited in the scintillator. Ignoring the effect of photon statistics, GEANT [18] simulations predicted an intrinsic resolution of $\Delta E/E = 6\%/\sqrt{E\,(\mathrm{GeV})}$, which could be improved somewhat by making the scintillator layers thinner and more numerous. Although cost was a factor, attenuation of light in the longest (up to 4.7 m) scintillator strips was the primary factor in choosing 10 mm for the thickness of the scintillator.

The choice of readout granularity was a compromise between the cost of photomultiplier tubes (PMTs), size constraints and resolution requirements. Good position resolution required that the transverse granularity be somewhat smaller than the lateral extent of the shower, but making it very much smaller appeared to have little value. Since the cost of PMTs was a major item in the detector budget, a careful optimization was necessary. The simulations indicated that a cell size of 10 cm would be a good compromise between resolution and cost.

In order to match the hexagonal geometry of the CLAS, the lead–scintillator sandwich is contained within a volume having the shape of an equilateral triangle. There are 39 layers in the sandwich, each consisting of a 10 mm thick BC412 scintillator followed by a 2.2 mm thick lead sheet. The calorimeter utilizes a 'projective' geometry, in which the area of each successive layer increases. This minimizes shower leakage at the edges of the active volume and minimizes the dispersion in arrival times of signals originating in different scintillator layers. The active volume of the sandwich thus forms a truncated triangular pyramid with a projected vertex at the CLAS target point 5 m away, and an area at the base of 8 m^2.

For the purposes of readout, each scintillator layer is made of 36 strips parallel to one side of the

triangle, with the orientation of the strips rotated by 120° in each successive layer (Fig. 2). Thus there are three orientations or views (labeled U, V and W), each containing 13 layers, which provide stereo information on the location of energy deposition. Each view is further subdivided into an inner (5 layers) and outer (8 layers) stack, to provide longitudinal sampling of the shower for improved hadron identification. Each module thus requires 36 (strips) × 3 (views) × 2 (stacks) = 216 PMTs. Altogether there are 1296 PMTs and 8424 scintillator strips in the six EC modules used in CLAS.

Our design uses a fiber optic light readout system to transmit the scintillator light to the PMTs. Fig. 3 displays a schematic side view and vertical cut of the fiber optic readout unit for a single inner and outer stack of the calorimeter module. As described later, these fibers were bent in a controlled way to form semi-rigid bundles originating at the ends of the scintillator strips and terminating at a plastic mixing light guide adapter coupled to a phototube. Because of the compound angles involved, each fiber bundle in a given detector module has unique dimensions.

The PMT and the light guide adapter are optically coupled using optical grease, while the light guide adapter is glued to the fiber readout bundle with a UV curing compound. The contact between the end of the scintillator and the fiber bundle, however, is made mechanically without optical coupling material at the joint. A special spring loaded expansion assembly is used to push the end locator, in which the fibers are glued, against the end of the scintillator. This coupling allows flexibility in positioning the scintillators in the containment box during assembly, and also prevents possible damage of the scintillator strips from thermal expansion.

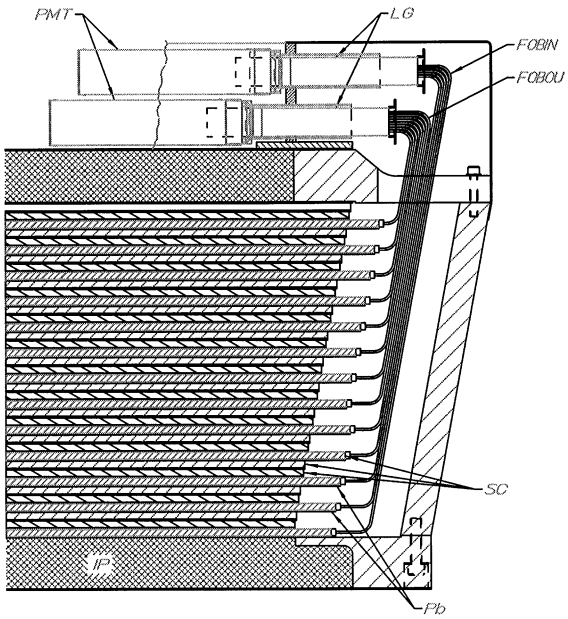

Fig. 3. Schematic vertical cut of EC light readout system. PMT – photomultiplier, LG –light guide, FOBIN – fiber optic bundle inner, FOBOU – fiber optic bundle outer, SC – scintillators, Pb – 2.2 mm lead sheets, IP – inner plate (composite: two 1.905 mm stainless steel face sheets and 72.2 mm foam core plate).

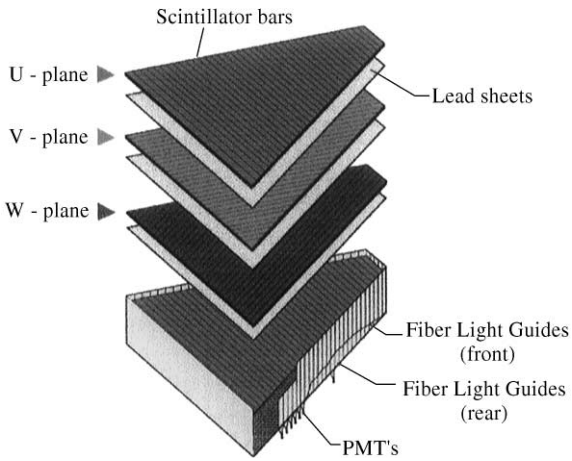

Fig. 2. Exploded view of one of the six CLAS electromagnetic calorimeter modules.

4. Electronics

4.1. Photomultiplier tubes

Photomultiplier tubes used in the calorimeter were selected for a linear response over the full operating range of deposited energy and count rate, and for time and amplitude resolutions good enough to have a negligible effect on the overall resolutions for the calorimeter.

The operating range was particularly important since the initial calibration of the calorimeter was performed with minimum ionizing particles (MIP), which deposit ≈ 2 MeV per scintillator, while an EM shower from a 6 GeV electron can deposit up to 2 GeV in the scintillators. Hence linearity over a dynamic range of 1000 : 1 was needed. Appropriate PMTs from several vendors were tested [3] and all showed excellent linearity over a 3500 : 1 dynamic range with a reasonable choice of high voltage, as well as good time and amplitude resolutions. For PMT pulses corresponding to a photoelectron yield of $n_{\mathrm{pe}} = 10^3$, which was the expected signal from a 1 GeV electron, the amplitude resolution was $\sigma_A/A \approx 4\%$, and the time resolution was $\sigma_t \approx 100$–150 ps (measured with a pulsed, variable intensity UV laser).

Following these tests, both Phillips XP2262 and EMI9954 PMTs were selected. Each PMT has a 42 mm diameter circular window, which is smaller than the 440 mm^2 area of the mixing light guide adapter. The high-voltage (HV) dividers are similar to a University of New Hampshire design used for the CLAS TOF counter PMTs [4]. The anode signal is split within the base so that the anode signals could be sent separately to the trigger and signal processing electronics.

The close packing of the six EC modules within the hexagonal geometry of CLAS made it necessary to mount PMTs on the back of the calorimeter to minimize the gaps between adjacent modules. Each PMT/HV divider assembly is contained in a plastic housing with a threaded collar that attaches to a flange on the aluminum can containing the mixing light guide. Each can is in turn glued onto a 'fence plate' on the backside of the calorimeter (see Fig. 3). A mu-metal insert provides magnetic shielding while electrical shielding is provided by an extruded aluminum can which fits over the plastic housing and makes electrical contact with all the connectors at the rear of the base. A hard connection to a common ground point inside the base is made via the screw which secures the shield to the plastic housing. Prior to installation all PMTs were checked for good gain stability and low noise.

Monitoring of PMT gains during data taking with beam is performed by measuring their response to light pulses distributed through optical fibers glued to the mixing light guide attached to each PMT [5]. The common light source is a small scintillator mounted at the center of each EC module, and excited by UV light from a nitrogen laser. About 10% of the primary laser light is deflected onto a photodiode, whose output is used to monitor the laser pulse intensity and to create a calibration trigger. Each secondary light source is also monitored relative to an ^{241}Am light pulser attached to one PMT per sector. This system allows relative PMT gain shifts to be measured to better than 5%.

4.2. Trigger and readout

The CLAS Level 1 hardware can form a trigger within 200 ns using prompt signals from each PMT-based detector package. Electron triggers require a signal based on the total energy deposited in the calorimeters. This is accomplished with a fast analog sum of all 216 PMTs in each EC module. The electronics, designed and built at the University of Virginia, are contained in single-width NIM modules that are designed to sum the 36 PMT anode signals belonging to the same U, V or W view. These signals are attenuated using removable resistors and summed internally in groups of six as shown in Fig. 4. The resistors are intended to compensate for the variations in average light attenuation arising from the large range of scintillator lengths. The summed signal is then integrated and clipped with a 30 ns delay line. The integration time (≈ 20–30 ns) is sufficient to accommodate the dispersion in arrival times arising from the EC triangular geometry.

Two other NIM modules provide further summing in various combinations. The first module creates U + V, U + W and V + W partial sums for both the inner and outer stacks, and the second module produces the inner and outer U + V + W sum and the total energy sum. CAEN C207 16 channel discriminators are used to convert these summed signals to ECL logic. Each channel has independently programmable input thresholds which allows different thresholds to be placed on the partial and total energy sums. The Level 1 electronics can be programmed to trigger on

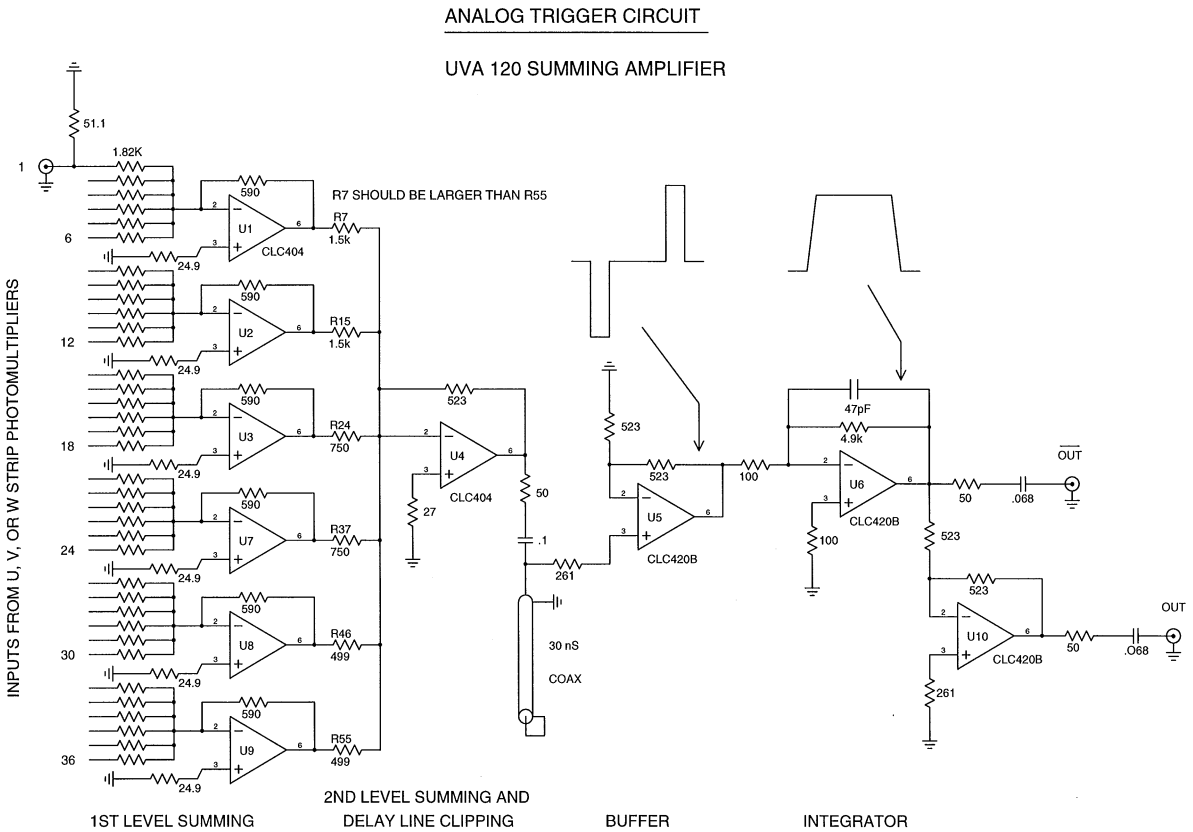

Fig. 4. Schematic of first stage summing amplifier used to create an analog energy sum for the CLAS electron trigger.

independent sectors using different combinations of energy deposition.

The second of the split anode signals from each PMT passes through a 420 ns delay cable to a passive splitter that divides the signal into two branches destined for TDCs and ADCs. The splitters, designed and built at University of Virginia, accommodate up to 64 channels per panel. Every splitter panel has four banks, each containing 16 channels. The input and output connectors are mounted on a common circuit board, with the input connectors available on the back of the panel to simplify cable routing. The input signal current is split in a 3 : 1 ratio with the higher value sent to the TDC discriminators. This ratio is designed to compensate for the higher sensitivity of the charge integrating ADC compared to the voltage-sensitive TDC discriminator. Miniature coaxial cable is used to transmit signals from the splitter to the TDC discriminators and the ADCs.

All 1296 PMT channels are read out with LeCroy 1881M ADC and LeCroy 1872A TDC boards. LeCroy 2313 leading edge discriminators are used to provide timing signals to the TDCs. Thresholds and output widths are typically set at 15 mV and 50 ns, respectively. The common start pulse for the TDCs is fed through the backplane. Channel-to-channel calibration is performed with a programmable pulser, with the average conversion gain set to 50 ps/channel. Both TDCs and ADCs are configured in sparcification mode to reduce data acquisition overhead. For TDCs, only channels receiving a stop pulse are read out, while for ADCs only channels producing a count above a preloaded threshold are read out. The threshold T applied to each ADC channel is

given by

$$T = A_{\mathrm{ped}} + \mathrm{constant}\,\sigma_{\mathrm{ped}} \quad (2)$$

where A_{ped} and σ_{ped} are the mean and RMS of the pedestal distribution for each channel. This serves to suppress both isolated noisy ADC channels and common noise from inductive pickup of local low-frequency EM fields. Typical thresholds of ≈ 15 channels are used, while the overall level of σ_{ped} is 3–8 channels. The ADC gate width is 200 ns, which is sufficient to accommodate the different arrival times of the EC PMT signals.

The detailed criteria for selection of the delay and trigger cables, readout electronics, discriminators and high-voltage system were dictated mainly by the CLAS TOF system and are described fully in Ref. [4].

5. Scintillators

Good energy and timing resolution required the use of a fast plastic scintillator with high light output and high transparency, along with an efficient light collection system. Following preliminary studies [6–9] of light yield, speed, transparency and cost, Bicron BC412 scintillator was chosen. A short summary of the scintillator studies and the light readout system are presented in this and the following section.

5.1. Description

The BC412 scintillator was cast at Bicron in large sheets from which the individual strips were cut before shipping. They were supplied in the form of 36 strips for each layer. These strips were 10 mm thick, approximately 100 mm wide, and with lengths covering the range 0.15–4.2 m. One end of the strip was cut at an angle to match the edge of the triangle and coated with a non-reflecting black material to minimize the effect of reflections. The other end was diamond milled at 90° to the axis of the strip, and will be referred to as the *readout end* in the following discussion. Before installation, each scintillator strip was measured to insure that the scintillation and optical properties as well as dimensional accuracy were within specifications. These measurements were subsequently used to improve the simulations and energy reconstruction software.

5.2. Light transmission

Light transmission was measured by exciting scintillations at various points along the length of each strip, while a PMT measured the response at the scintillator readout end. To test the large number (≈ 8500) of scintillator strips in a reasonable time, several test setups were developed and operated in parallel. Scintillator strips shorter than 3.0 m were measured using a 250 kW UV ($\lambda = 337.1$ nm) pulsed nitrogen laser in an arrangement that permitted six strips to be tested simultaneously. The laser pulse was fanned out through quartz fibers to six parallel sets of 29 test points 10 cm apart. Computer-controlled shutters allowed the laser light to sequentially illuminate various points on each of the six scintillator strips. Scintillator strips longer than 3.0 m were measured using various sources (a radioactive source, an X-ray source, or a fiber to transport UV light) attached to a cart that moved along a track parallel to the scintillator strip. Although this method was slower, the use of a single, local source provided an absolute measurement. A similar apparatus was used to cross-calibrate the laser-driven setup. Details are described in Ref. [9].

Typical dependence of the readout PMT anode current on the source position for a 4 m long scintillator strip is shown in Fig. 5. A collimated 0.5 mR ^{60}Co γ source was used to excite the scintillator. The region of excitation was measured with a scintillator rod to be ≈ 4.5 cm (FWHM). The current is seen to abruptly drop to PMT dark current levels when the source reaches the far end of scintillator. This background, which is almost 13% of the scintillation signal at this point, was subtracted from all measurements prior to fitting. The overall RMS uncertainty in the current measurement was 1.5%.

A sum of two exponentials was sufficient to describe the scintillator attenuation response:

$$A = A_1 e^{-x/L_1} + A_2 e^{-x/L_2} \quad (3)$$

where L_1 and L_2 are the attenuation lengths of the two observed components. After measurements of

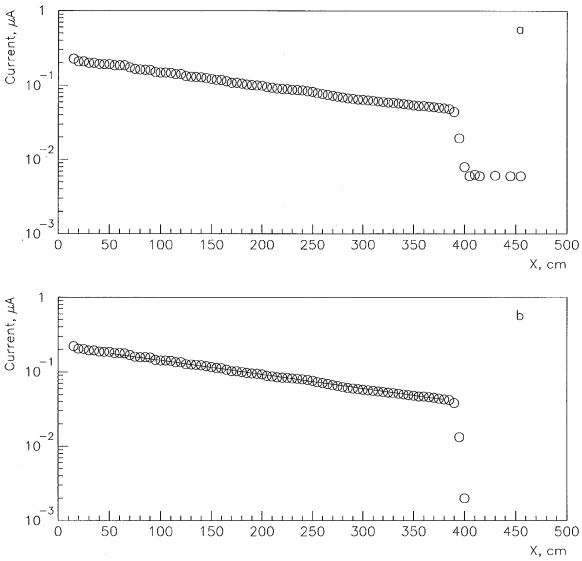

Fig. 5. PMT anode current dependence versus ^{60}Co source position along a 4 m long BC412 scintillator strip with direct readout. (a) Measured response. For $x > 400$ cm only PMT dark current contributes. (b) Same as (a) with dark current subtracted. Fitted parameters from Eq. (3) are $L_1 = 40$ cm, $L_2 = 250$ cm and $A_2/A_1 = 0.22$.

about 100 strips it was found that $L_1 \leq 50$ cm, $\langle L_2 \rangle \approx 250$ cm and the ratio $A_1/A_2 \leq 0.5$. Thus, the influence of the first component at the distance of $x \approx 50$ cm was no more then 20% and for $x \geq 50$ cm the response could be fitted with a single exponential:

$$A = A_0 e^{-x/L_0}. \tag{4}$$

The fits of data for 100 strips using both Eqs. (3) and (4) showed that $L_0/L_2 = 0.98 \pm 0.03$, and that the attenuation length of Bicron BC412 scintillator satisfied the calorimeter specification: $L_0 \geq 220$ cm for strips longer than 300 cm.

After completing the preliminary tests, the measurement apparatus for the longest strips was changed by replacing the direct coupling of the scintillator to the photomultiplier with a fiber optics coupling to make the measurements consistent with the fiber optics readout method chosen for the calorimeter.

As discussed later, fiber optics readout increases the measured attenuation lengths for strips longer than 4 m by 15%. The results for all the calorimeter scintillators are shown in Fig. 6.

5.3. Absolute light yield

The fraction of the scintillation light reaching a PMT needed to be large enough to ensure that the energy resolution was not dominated by photoelectron statistics.

To measure the scintillator output, a 1 cm diameter radioactive ^{207}Bi source was used to excite the scintillator. The 1 MeV conversion electrons were completely absorbed in the scintillator. The signals were tagged with a PMT on the other side of the scintillator directly opposite from the source. Another PMT coupled directly to the end of the scintillator measured the light reaching the end of the strip. The number of photoelectrons was large enough for the observed spectrum to be Gaussian so that the number of photoelectrons (normalized to 1 MeV) could be determined by

$$n_{pe} = \frac{\Delta S}{S} \frac{A_G}{a_1} \tag{5}$$

where A_G is the centroid of the Gaussian, S is the surface area of the end of the scintillator from which the light is emerging, and ΔS is the portion of this surface covered by the PMT photocathode ($\Delta S/S \simeq 0.44$). The parameter a_1 represents the response to a single photoelectron, which was determined by attenuating the light and fitting the PMT anode pulse height spectrum to a sum of Poisson-weighted Gaussian distributions. Using Eq. (5) the photoelectron yield obtained with direct readout was approximately 200/MeV. Later we discuss the photoelectron yield obtained with the fiber optics readout system.

5.4. Time response

The time resolution depends on the decay time τ of the scintillators, on fluctuations in the length of the light path to the PMT, on photoelectron statistics, and on intrinsic properties of the PMT itself. To determine τ, the time difference between the anode signal of the tagging PMT and that of the readout PMT was measured, after attenuating the

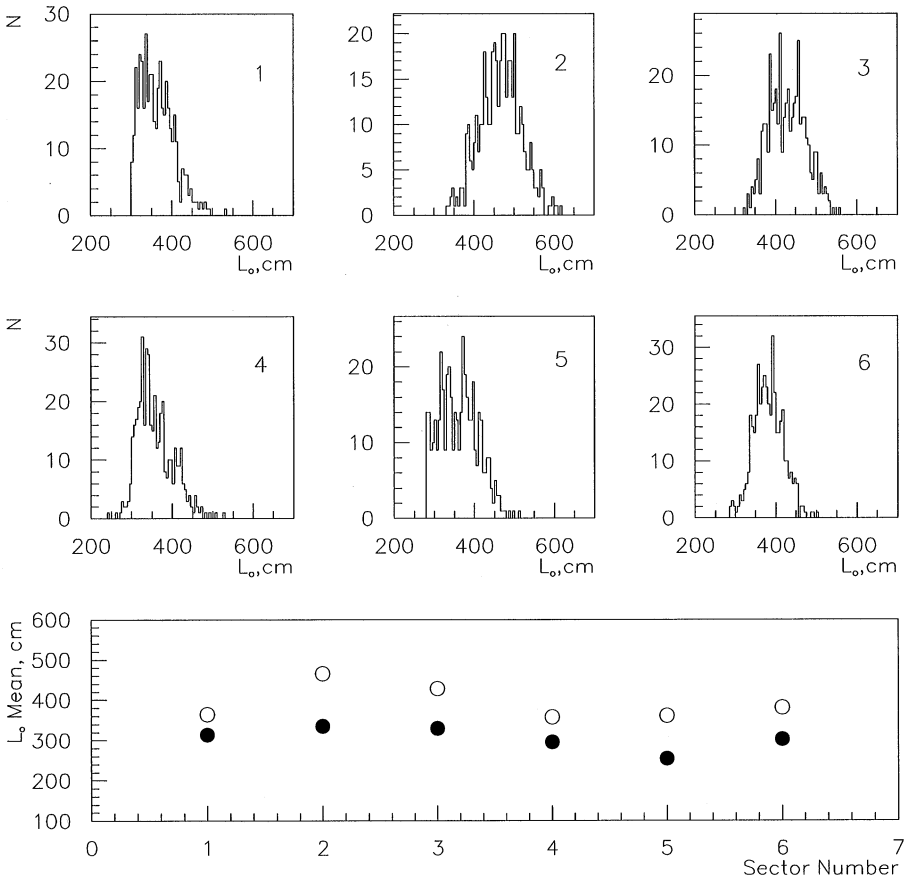

Fig. 6. Top: Attenuation length of strips for all six sectors for scintillators having length $x \geqslant 300$ cm. Bottom: $\langle L_0 \rangle$ for each sector. Open and dark circles for strips with $x \geqslant 300$ cm and $k = 150$–300 cm, respectively.

readout light so that $n_{pe} \ll 1$. The time spectrum was fitted to an exponential, which yielded $\tau = 3.6$ ns. This value is slightly larger than specified by Bicron ($\tau = 3.3$ ns) for the BC412 scintillator [10]. This difference is at least partly due to time jitter in the readout PMT arising from small photoelectron statistics ($\simeq 300$ ps) and partly due to the transit time variations of photoelectrons ejected from different portions of the PMT photocathode ($\simeq 700$ ps).

5.5. Other characteristics

The life expectancy of the CLAS detector is 10–15 years. The expected total dose of radiation from EM showers over 10 years could be as much as 100 Gy. To be sure that the BC412 scintillator would survive such a dose, a 2 m long strip was tested [11] to estimate the radiation-induced effects on the absolute light output and attenuation length. The strip was irradiated by a ^{60}Co line source at the rate of 0.5 Gy/h, which is sufficiently low to allow complete diffusion of oxygen into the material during the irradiation. In addition, a pure oxygen atmosphere was circulated around the strip during the radiation to insure complete diffusion and to produce a pessimistic estimate of the damage. The strip was irradiated over 320 h for a total dose of 160 Gy. Measurements before and after the irradiation showed no loss in absolute light output, and a decrease of only 16% in the attenuation length over the full 2 m length. Therefore, it was

concluded that any deterioration over the life time of the detector from its radiation dose would be negligible.

It is well known that the surfaces of some scintillators, especially mechanically machined ones, can gradually develop micro-cracks, which can dramatically decrease the attenuation length. To check for such deterioration, some BC412 scintillator strips tested at the end of 1991 were re-tested in 1995. No significant changes in the scintillation and transmission characteristics were discovered.

The differential thermal expansion of the scintillators was measured for various loading conditions ranging from no load to the full 90 g/cm^2 expected at the bottom of the outer stack. A 1.5–2 mm change in the length of a 3.2 m long scintillator strip was observed when it was heated by 12°C, about 60% smaller than expected from the cited coefficient of thermal expansion [10] of 7.8×10^{-5}°C^{-1}.

For good timing and uniformity, the scintillator light should be propagated with total internal reflection at the surfaces. To isolate the scintillators optically from each other and to protect them from the lead, an opaque wrapping that was not optically coupled to the surface was required. Also some parts of the scintillators are under high pressure ($\approx$90 g/cm^2) from the layers above them. To study the effect of this loading, the light yield and attenuation properties were measured with the scintillator wrapped in different materials and with pressure applied to the scintillator surface. For the maximum pressure expected in the calorimeter there were several materials for which no noticeable ($<$5%) changes in light output could be observed. We chose to use 75 μm thick Teflon tape.

6. Light collection system

The main considerations in the design of the light collection system are as follows:

(1) the photomultiplier tubes must be located at the rear of the detector to maximize the sensitive area;
(2) separate readout for the inner and outer, stacks of the calorimeter;
(3) a single PMT was to be used to readout 5 (8) successive strips in the inner (outer) stacks;
(4) Accommodation of the projective geometry;
(5) the light transmission to the PMTs should be high enough to play no significant role in the energy resolution of the detector;
(6) preservation of the quality of signal timing;
(7) allowance for thermal expansion and contraction of the scintillator.

Two coupling systems seemed to meet most of these requirements, one using a wavelength shifter (WLS) and another using fiber optics. Readout with a single plastic WLS strip mounted perpendicular to a scintillator stack could be used to readout 5 (or 8) successive calorimeter strips. A small air gap between the scintillators and the WLS would ensure that the shifted light would propagate by total internal reflection to the end of the WLS strip where a PMT was optically coupled. Another scheme used plastic optical fibers to transport the light from the scintillator to a PMT. The advantages of flexibility, high light transmission and fast time response made fiber coupling an attractive alternative to WLS. However, limitations on the number of fibers that could be used and the reduction in the angular range for total internal reflection in the fibers as compared to WLS caused concern.

As part of our studies, a prototype calorimeter using WLS strips was built and tested [8]. Extensive measurements were also made to compare the two methods and are discussed in the following sections.

6.1. Light transmission

The photoelectron yield n_{pe} was measured for both WLS and fiber readout systems. Four types of WLS were tested: G2, BC482, BC499, and NE172, each 60 cm long with a cross-section of 10.0 cm^2 (10 cm × 1 cm). A bundle of 60 plastic BCF98 (Bicron) fibers, 50 cm long and 2 mm in diameter with one 90° bend was also tested. For all the tests the signal at the PMT was normalized by comparison to a signal from a PMT attached directly to the scintillator.

The average measured photoelectron yields are summarized in Table 1. The reduction in n_{pe} for WLS compared to the direct readout case was primarily due to the small fraction of the

Table 1
Photoelectron yield n_{pe} and average decay time τ from BC-412 scintillator for various readout systems

Light readout	n_{pe} (MeV^{-1})	τ (ns)
Direct	≈ 200	3.6
WLS G2	6.1	5.1
WLS BC482	7.8	8.7
WLS BC499	6.8	7.4
WLS NE172	7.6	6.1
BCF98 fiber readout		
18.8% coverage	8.4	3.6
BOF98 fiber readout		
Max (78%) coverage	≈ 35	—

Table 2
Attenuation performance of 4 m long BC412 scintillator with various readout systems, the variables A_1, A_2, L_1 and L_2 are defined by Eq. (3)

System	A_1/A_2	L_1	L_2
Direct	0.54 ± 0.003	47 ± 0.7	274 ± 0.9
WLS G2	1.26 ± 0.008	28 ± 0.1	186 ± 0.5
WLS BC482	0.92 ± 0.009	34 ± 0.4	206 ± 1.1
WLS BC499	0.87 ± 0.007	33 ± 0.8	221 ± 1.1
WLS NE172	0.96 ± 0.006	28 ± 0.3	220 ± 0.6
Fibers	0.4 ± 0.006	52 ± 1.3	326 ± 2.1

isotropically re-emitted light transmitted to the PMT, and to the decreased sensitivity of the photocathode to the green light emitted by the wavelength shifter (QE at 510 nm $\simeq$ 10%, while at 430 nm $\simeq$ 20%). The highest n_{pe} was obtained with BC482, for which $n_{pe} = 7.8$/MeV.

Using a 60 fiber bundle covering 18.8% of the scintillator end surface resulted in $n_{pe} = 8.4$/MeV [11]. In principle, it is possible to obtain 78% coverage with 2 mm fibers (70% for 3 mm fiber), which would yield $n_{pe} \approx 35$/MeV (see the last row of Table 1). However, since the total readout surface area from 5 (8) scintillators is ≈ 3 (5) times larger than the active surface of the XP2262 PMT photocathode, the maximum number of photoelectrons/PMT that could be collected with fiber coupling is $n_{pe} \approx 12$ (7)/MeV, comparable to the result achieved with WLS. Therefore, light transmission does not clearly favor either technique.

The observed reduction in n_{pe} of $\approx 0.78 \times 200/35 = 4.5$ for fiber readout compared to direct readout arises largely from the smaller acceptance angle θ_a for total internal reflection in BCF98 fiber ($\theta_a = 21^\circ$) compared to BC412 scintillator ($\theta_a = 51^\circ$), due to the fiber cladding. A simple calculation of the reduced acceptance $1 - \cos 51^\circ / 1 - \cos 21^\circ \approx 5.6$ somewhat overestimates the measured value.

6.2. Time characteristics

The effect of the light readout method on the time resolution of the calorimeter was investigated by measuring the scintillation decay time in the same way as for the direct readout case (see Section 5). Results are given in Table 1. For the fiber optics readout, the time spectrum was identical to that obtained with direct readout, as was expected since there is no significant dispersion in the optical fibers. The longer decay time for WLS was due to the slowness of the wavelength shifting fluor, and was large enough to have a significant effect on the timing resolution for minimum ionizing particles, low-energy photons from π° decay, and neutrons, all of which produce a low number of photoelectrons. Thus, on the basis of timing resolution, the fiber optics readout was clearly superior.

6.3. Light attenuation

The effective attenuation length of a scintillator is also affected by the readout technique. The results are summarized in Table 2. The WLS readout reduced the effective attenuation length by at least 20%, whereas the optical fiber readout increased it by (≈ 18%, relative to that obtained with direct coupling. The increased attenuation obtained with WLS simply results from WLS being more sensitive to shorter wavelength light for which the scintillators are less transparent. On the other hand, the optical fibers are equally transparent to all visible wavelengths, but have an acceptance angle less than that for the scintillator, so the fibers accept only a fraction of the internally reflected photons ariving at the end of the scintillator. Since these have traveled through the scintillator with fewer reflections than the rejected ones, they

have a shorter path length, which results in less attenuation.

Taking into account all these tests, it was decided to use the fiber readout system.

6.4. Fabrication and testing

After testing several types of optical fiber, the 3 mm Bicron BCF98 fiber was chosen. Bundles using this fiber were sufficiently flexible to allow for thermal expansion, while the cladding of the fibers assured continuity of performance over a long period of time. Although 2 mm diameter BCF98 fiber is more flexible, it has a higher cost per unit length, while covering the same readout surface increases the total fiber length by $\frac{9}{4}$ (note that in the calorimeter ≈ 80 km of 3 mm fiber is used).

For six calorimeter modules, 1296 fiber bundles had to be prepared, containing a total of 185,238 fibers. Because of the projective geometry of the calorimeter, fiber bundles with different lengths and with bends having different azimuthal and polar angles were needed. For this purpose, special bending machines were designed and built at Jefferson Lab. Furthermore, an efficient method for bending them without damaging their transmission properties was required. Our studies showed that the best method was to bend the fibers in an atmosphere of air after heating them to 105–110°C. Two large-volume commercial ovens with very uniform (± 1°C) inside temperature distribution were used. The best results were obtained with Bicron BCF98 fibers. With two bends of $\approx 90°$ the light transmission in the 400–550 nm region was 85–90% of that of the untreated straight fiber. After the initial tests of light transmission, some of the bent fibers were stored for two years and re-tested. No changes in the transparency could be detected.

A total of 22 fibers was used to cover $\approx 14\%$ of the end surface of each scintillator. These 22 fibers were glued into holes drilled in a rectangular aluminum holder with a cross-section $\approx 80\,\mathrm{mm}^2$. For the inner part of the calorimeter, 5 sets of 22 fibers were potted together in aluminum frames using a black glue. For the outer part of the calorimeter, 8 sets of 22 fibers were potted together. The readout end has a rectangular cross-section of $20 \times 85\,\mathrm{mm}^2$ for the five-scintillator bundle and $40 \times 85\,\mathrm{mm}^2$ for the eight-scintillator bundle. The total fiber area is 780 (1240) mm^2 for the inner (outer) readout bundles. A diamond cutter was used to mill both ends of the fiber bundle to produce a smooth, optically transparent surface. All 1296 bundles were constructed over a period of 3.5 years.

The optical transmission of every fiber bundle was tested using a UV light source. The acceptance criteria was that the transmission of individual fibers should not deviate more than 15% from the average transmission of the bundle. About 9% of the bundles were rejected.

A lucite light guide was used to couple the readout ends of the fiber bundles to the circular PMT photocathode, which had an area of $1400\,\mathrm{mm}^2$. The light guide also served to distribute the light from any fiber over the entire PMT photocathode. According to a GEANT simulation, a geometrical efficiency of 95% could be obtained with an adapter 27 cm long. Measurements showed that 85% of the light was transmitted and that the total efficiency of the light guide (product of transmission and geometrical efficiency) was $\approx 80\%$.

6.5. Light yield and time resolution tests using fiber readout

One of the fiber bundles described above was used with a mock-up of one of the outer calorimeter stacks to check the absolute light yield and time resolution. Each of the 8 scintillators in the mock-up was successively irradiated by a ^{207}Bi source placed 15 cm from the readout end. The average photoelectron yield n_{pe} from the PMT cathode was approximately 3.4/MeV, significantly less than estimated from the earlier test measurements (8.4/MeV, see Table 1). Several effects can account for this difference:

- the light guide adapter had a net efficiency of 80%, instead of 100%;
- fiber coverage of the scintillator end was 14%, instead of 18.8%;
- transmission through the doubly bent fibers was 90%;
- distance from the irradiation point to the PMT was 5 cm longer, resulting in a 10% attenuation ($\exp(-5/50) = 0.9$).

Taken together, these effects reduce the expected yield to $n_{pe} \approx 4/\text{MeV}$, which is only 20% higher than the measurement.

The timing resolution of this prototype stack was measured by placing trigger counters above and below the stack to select cosmic-ray muons passing completely through the stack. The mean time difference between the PMT attached to the fiber readout system and one of the trigger PMTs was measured, yielding a time resolution of $\sigma_t \approx 0.5$ ns.

7. Assembly

7.1. Mechanical support

The selection of the mechanical support system for the calorimeter components was constrained by several considerations. First, it was desirable to minimize the amount of inert material traversed by the particles, while still supporting 17 tons of material per module. Second, there were issues of differential thermal expansion since the components of the detector included metals and plastics in proximity in lengths of up to 5 m. Lastly, the design had to accommodate variations in the dimensions of the constituent materials.

The mechanical structure containing the lead–scintillator layers consisted of large-area upper and lower triangular plates made of aircraft-grade composite material, supported on edge by a triangular box fabricated of three solid aluminum plates 3.165 cm in thickness. The composite plates consisted of 10 cm of polyurethane heavy construction foam epoxied to a 0.15875 cm stainless steel skin above and below; the edges of each plate were reinforced by solid aluminum bars. In this manner the total thickness of material traversed by entering particles is limited to approximately one radiation length of stainless steel, yet the structure itself is exceedingly strong. When, supported at the edges and loaded with a weight equivalent to a distributed weight of 17 tons, the horizontal deflection was measured to be 0.635 cm, in agreement with calculations. The assembly tolerances of the box structure were maintained to 0.5 mm at 21°C.

The differential thermal expansion of the long scintillator strips was accommodated by supporting each strip on the readout end by a spring assembly designed to support up to the full weight of the scintillator. This design allows up to 3 mm of expansion, corresponding to a temperature variation of 7.7°C for a 5 m long scintillator. The expansion springs were mounted into threaded holes in the wall of the box, permitting final tensioning after all scintillators had been installed. The spring force was transmitted to each strip by the same assembly which holds the light guide, ensuring positive contact between the light guide and the strip during expansion and contraction.

Some of the scintillator dimensional tolerances were significant cost drivers. An example is the scintillator thickness, which was permitted to vary over a range of as much a $\pm 5\%$. In the assembly procedure these variations were compensated by mechanical shims: paper sheeting for the thickness variations, solid aluminum pieces for the length variations, and Teflon strips for the width variations.

7.2. Lead-scintillator stacking

The stacking procedure consisted of installing alternating layers of lead and scintillator strips into the mechanical support box, including shimming, alignment, and installation of the light guide attachment structure. Considerations requiring particular care included protection of the scintillator surface from abrasion by contact with the lead sheets, the control of dust particles and chemical contaminants, precision placement of the scintillator strips, control of dimensional precision for the lead sheeting, and control of the cumulative stack height in the presence of thickness variations of the lead and scintillator.

To prevent abrasion of the scintillator surfaces by the lead metal, clean virgin Teflon sheeting 0.00762 cm in thickness was used to separate the two materials, and the lead sheets were thoroughly cleaned and any protrusions removed. A closely related problem was the control of dust particles. Dust particles in contact with the scintillator surface will produce extended scratches as the strip expands and contracts with varying temperature. To avoid this, standard clean-room techniques were employed to limit the amount of dust

available; in addition, the scintillators were installed only onto freshly installed Teflon sheeting, and the scintillators were never left uncovered for any length of time, including during the measurements of the attenuation lengths which were performed for each strip. Teflon strips were also installed between the scintillators, so that they were completely surrounded by this inert material on all sides. This provides both mechanical protection as well as isolation from chemical contamination, which was further ensured by careful cleaning of all other components as well as continuous nitrogen flushing of the inside volume of the detector.

The placement of individual scintillator strips was controlled to within 3 mm in order to preserve the expected position resolution. The dimensions and placement of the lead sheets were typically controlled to 0.5–1.0 mm in order to have uniform mechanical support of the lead as well as to minimize any gaps. The cumulative stack height was monitored and compensated both by thin paper shims as well as by selection of the lead sheets, whose thicknesses were measured over their full area in order to avoid excessive accumulated thickness.

7.3. Light guide installation

The fiber light guide bundles were added to each detector module after the completion of the stacking by removing one of the three 'walls' of the box and sliding the light guide into place. The wall was then replaced, and after all light guides were installed the expansion springs were tensioned.

8. Simulations and event reconstruction

8.1. GEANT simulation

Early GEANT studies [12,13] of the EC were used in combination with prototypes to provide guidance in the original design (particularly with respect to segmentation of readout) as well as the development of the reconstruction software. A typical simulated EM shower initiated by a 2.4 GeV electron is shown in Fig. 7. The transverse and longitudinal development of the shower is evident, and the figure also shows a small amount of shower leakage from the rear, as well as backscattered photons emerging from the front.

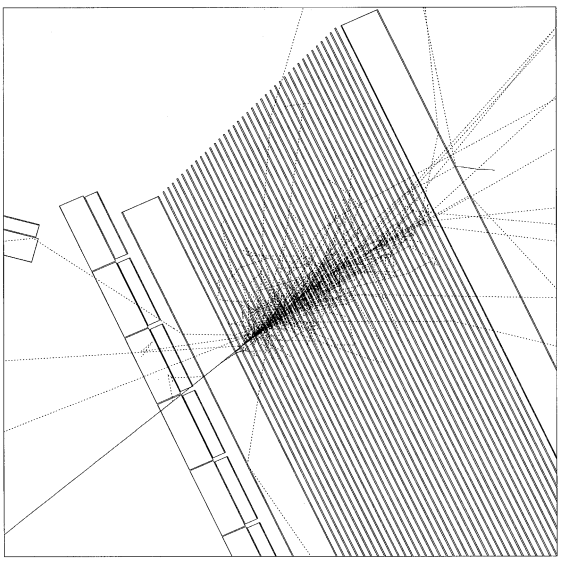

Fig. 7. GEANT simulation of EC response to 2.4 GeV electron. Electron enters picture from lower left. Dotted lines show photons emerging from shower. Also shown are individual TOF bars and backing structure. Energy loss in these structures as well as front EC cover plate is included in the simulation. Individual lead sheets of the calorimeter are shown. EC scintillators are not shown.

Some basic features emerging from these studies can be summarized:

- about 95% of the shower is concentrated within a 4 cm transverse diameter;
- for electron energies ranging between 0.5 and 4.5 GeV, the longitudinal shower profile peaks between layers 6 and 12 (out of 39);
- over the same energy range, shower leakage from the rear amounts to 0.8–2.2% of the total shower energy.

As a result of these simulations, the transverse granularity of the three-fold stereo readout was established. This is displayed in Fig. 8, where the EM shower is seen to be well localized using the design segmentation. GEANT simulations also fixed the longitudinal division of the calorimeter readout into 13 inner layers and 26 outer layers, to take advantage of the different energy deposition profiles for MIP tracks and EM showers.

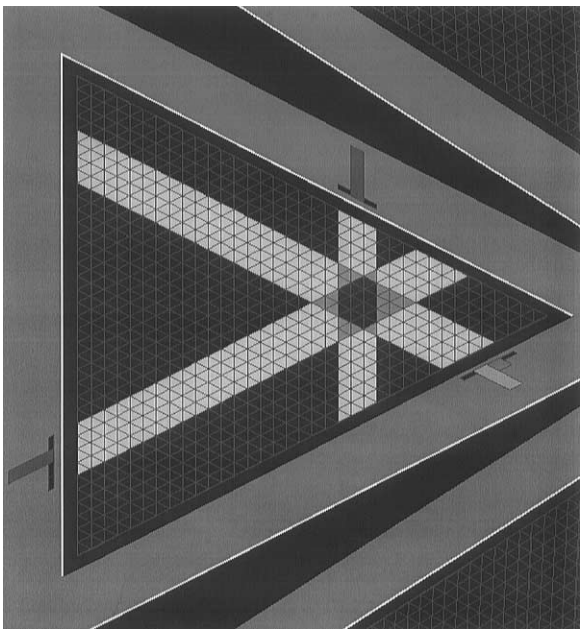

Fig. 8. Single event display of GEANT simulated EM shower in EC. Energy deposition profile is shown along each of the U, V, W views (outer stacks not shown). Individual scintillator strips are ≈ 10 cm wide.

8.2. Event reconstruction

Particle interactions within the calorimeter generally fall into the following categories, listed in order of increasing complexity of reconstruction:

(1) minimum ionizing,
(2) electromagnetic showers,
(3) hadronic interactions.

The reconstruction software must contain several components: First, fast and efficient pattern recognition that can distinguish the physical processes listed above, identify multiple hits and also reject noise. Second, energy reconstruction that corrects for light attenuation in the scintillators, position and energy dependencies of the sampling fraction and ambiguities arising from overlapping hits or multiple hits sharing a single PMT readout channel. Third, time reconstruction that provides a resolution comparable to the SC or CC counters, which can be used to determine neutron energy through time of flight, provide particle ID for other charged particles, and serve as a redundant measure of the trigger time for electrons.

We chose a simple pattern recognition algorithm [14] that takes advantage of the unique geometry and stereo readout features of the EC. As discussed earlier, the 39 scintillator *layers* within the EC lead: scintillator sandwich are transversely sliced into 36 *strips*, with the shortest strip labeled 1. The slice direction rotates by $\approx 120^\circ$ for each layer, providing three *views* labeled U, V and W. For each strip within a view, 5 layers are optically ganged into an *inner stack* (closest to the target) and 8 layers are ganged into an *outer stack*. Individual PMT readout of the inner and outer stacks is provided.

To reconstruct a typical EM shower event as shown in Fig. 8, the software first identifies groups, or collections of strips in each of the three views (U, V, W). Strips are placed in groups if: (1) the PMT response is above a software threshold and (2) the strips are contiguous. The groups are then re-sorted according to the sum of the strip energies (uncorrected for attenuation) and the centroid and RMS for each group is calculated. These grouped strips are called *peaks*.

After the initial guess for the peaks in each view has been defined, the algorithm next tries to match them together into *hits*. The criterion for a hit is that a collection of peaks satisfy the triangle sum rule. (For an equilateral triangle the triangle sum rule requires the sum of the U, V, W peak coordinates, measured from the corner, to be constant.) First, a three-fold loop looks at all possible combinations of peaks in the U, V, and W views. For each iteration of the loop, the triangle sum rule is checked as a test for a geometrically plausible event, using the centroids in each of the three views and the RMS as an estimate of the peak position uncertainty. If the condition is satisfied the path from the hit position to the PMT is calculated for each strip in the matched group, and the peak energy is corrected for scintillator attenuation. Peak centroids, RMS and higher moments are then recalculated.

Next, peaks which are part of more than one hit are treated. If for all hits there is only one peak in each view, then the routine proceeds to the next step. If a given peak contributes to multiple hits, then the energy in each hit due to that peak is

calculated as being proportional to the relative sizes of the multiple hits as measured in other views. That is, if there are two hits, both of which have the same 'U' peak, the energy in V and W is added for each of the hits, and the ratio of these summed energies determines how much of the u peak's energy is assigned to each of the two hits. The code does not attempt to handle more complicated events, which, of course, are topologically possible.

The hit is then again checked for the triangle condition, using the refined (attenuation-length-corrected) centroid and RMS values. Next the hits are sorted by energy, and another threshold cut is applied (which is a true energy threshold since attenuation corrections have already been applied). Software thresholds applied at the strip, peak and hit level are 1, 3 and 10 MeV, respectively.

8.3. Sampling fraction and resolution

The total energy deposited in the scintillators, expressed as a fraction of the incident particle energy, is the *sampling fraction* f_s. For a sampling calorimeter this ratio is less than 1 and depends on the ratio of active to passive material, as well as the total thickness. Knowledge of this quantity is important to understanding the absolute energy calibration. For our purposes, we estimate f_s using the *reconstructed* energy, for which f_s depends also on scintillator quality and software reconstruction algorithms.

Another important parameter in calorimeter performance is resolution. It is well known that the dominant contribution to the energy resolution σ/E comes from fluctuations in the number of secondary particle tracks sampled. This contribution can be expressed as

$$\sigma/E \propto \sqrt{t_s/f_s} \tag{6}$$

where t_s is the sampling thickness measured in radiation lengths. Fluctuations due to shower leakage from the rear of the calorimeter can also contribute. Previous GEANT studies [12] of the EC determined these components by fixing t_s but varying the number of layers and found $\sigma_{fs}/E = 0.068/\sqrt{E\,(\mathrm{GeV})}$ and $\sigma_{\mathrm{leakage}}/E = (0.016 - 0.019)\sqrt{E\,(\mathrm{GeV})}$.

Simulation results are summarized in Fig. 9, which shows both the sampling fraction and resolution expected for EC. For these plots electrons were generated from the target position and allowed to bend through the CLAS toroidal magnetic field and pass through the detector materials before striking the calorimeter. The electrons were thrown uniformly in θ and ϕ, in order to fill the calorimeter acceptance.

The upper panel of Fig. 9 indicates a dependence of f_s on the electron energy. (The symbols refer to simulations run under various conditions to be discussed shortly.) Some of this dependence can be attributed to ionization losses by the electron in the materials immediately preceding the sandwich (see Figs. 3 and 7), such as the TOF scintillators, backing structure and the front cover plate of the calorimeter box. The ionization energy losses in these materials are listed in Table 3, and the expected effect on f_s is given by the curved line in Fig. 9. Total thickness of these materials is about

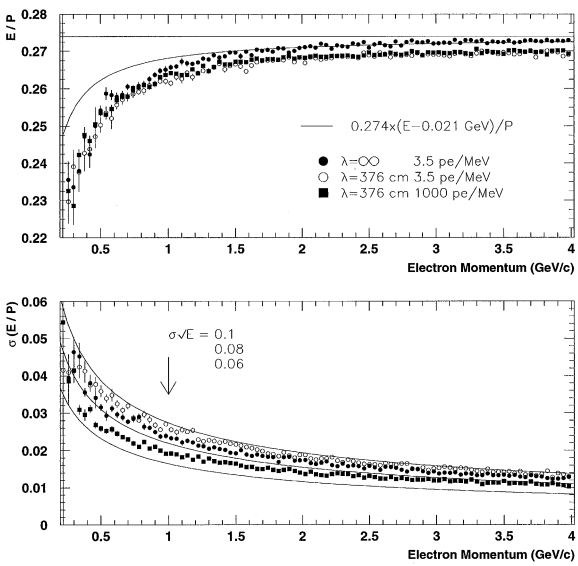

Fig. 9. GEANT prediction for sampling fraction (E/p) and resolution σ of EC module. Top panel: Ratio of reconstructed energy E to electron momentum p versus p. Symbols denote simulations run under different assumptions about scintillator attenuation length λ and light yield. Curve shows expected E/p from upstream $\mathrm{d}E/\mathrm{d}x$ losses. Bottom panel: $\sigma(E/p)$ versus p. Curves assume resolution varies as $a/\sqrt{E}$, where $a = 0.1$, 0.08 and 0.06.

Table 3
Materials present in the TOF bars, support structure, EC cover plate and used in GEANT simulation (see Fig. 7). Energy losses ΔE are calculated for minimum-ionizing particles (MIP)

Material	Thickness (cm)	ΔE (MIP) (MeV)	Total (MeV)
Lead	0.013	0.167	0.167
Polyvinyltoluene	5.0	10.1	10.3
Stainless steel	0.152	1.74	12.0
Polyurethane	2.54	0.37	12.4
Stainless steel	0.152	1.74	14.1
Stainless steel	0.16	1.84	15.9
Polyurethane	7.62	3.29	19.2
Stainless steel	0.19	2.18	21.4

1 radiation length, so they behave as a pre-radiator for the calorimeter. The discrepancy between the ionization energy loss model and the simulated f_s dependence for electron momenta below 1 GeV/c is not completely understood. However for these momenta, photons from radiative energy loss have energies corresponding to large Compton cross-sections, and are possibly backscattered out from the calorimeter before initiating an EM shower.

Several simulations were run assuming different parameters for the light collection: transparent scintillators ($\lambda = \infty$), constant attenuation length ($\lambda = 376$ cm) and large light yields (1000 pe/MeV). Fig. 9 shows that there is a small decrease in f_s for ($\lambda = 376$) compared to completely transparent scintillators, since light attenuation can cause the signal to drop below reconstruction software cuts and hence fewer strips contribute to the hit. Transparent scintillators also improve the resolution (bottom panel) by increasing the number of photoelectrons detected. The contribution to our resolution from photoelectron statistics can be seen by comparing the case where it is negligible (1000 pe/MeV) to the case of our expected photoelectron yield of 3.5 pe/MeV. Overall we expected a resolution $\sigma/E = (0.085 - 0.095)/\sqrt{E\,(\mathrm{GeV})}$.

9. Energy calibration

The CLAS electron trigger is normally configured to accept only events which deposit more than minimum ionizing energy in the calorimeters, which together with the Cherenkov counters help to reject pions. This requirement demands that the EC response to a fixed deposited energy be independent of the position of the hit, otherwise the trigger threshold is ill-defined and the trigger response will be non-uniform near threshold. Therefore, it was necessary to obtain a uniform and accurate energy calibration prior to taking production beam. A procedure using cosmic-ray muons was developed to perform the initial gain matching of the PMTs and is discussed below.

9.1. PMT gain matching and attenuation length corrections

Since the energy of an electron tracked through the CLAS detector and incident on the EC module is known, energy calibration of the EC is in principle possible by adjusting individual PMT gains until the reconstructed energy matches the known energy. Due to the longitudinal and transverse segmentation of the calorimeter readout, as well as the triangle rule requirement for pattern recognition, most reconstructed hits in the EC involve a minimum of 6 PMTs. The reconstructed energy, E_{tot}, represents a sum over a minimum of 13 unknown quantities, as follows:

$$E_{\mathrm{tot}} = \sum_{s}^{2}\sum_{v}^{3}\sum_{n}^{N} E_n^{sv}/f_s \tag{7}$$

$$E_n^{sv} = G(A_{\mathrm{sig}} - A_{\mathrm{ped}})/\exp(-x/\lambda) \tag{8}$$

where E_n^{sv} is the energy seen by the nth PMT contributing to the peak in view v and stack s. The unknown quantities are the PMT gains G, effective attenuation lengths λ and the overall sampling fraction f_s. The summation occurs over the N PMTs in each view, over the 3 U, V, W views for each stack, and over the inner and outer stacks. A_{sig} is the ADC channel corresponding to the digitized PMT-signal, A_{ped} is the ADC pedestal and x is the PMT-reconstructed hit distance.

Due to the energy sharing between PMTs enforced by the three-fold stereo readout, determination of the quantities G, λ and f_s is a more complicated problem compared to conventional readout geometries. The relationship between the total

deposited energy E_{tot} and the partial energies E_n^{sv} is non-trivial for EM showers. A global optimization approach would require fitting 433 parameters per sector and might be very slow to converge.

Another approach is to proceed iteratively, using minimum ionizing particles (MIP) such as cosmic muons to simplify the energy deposition profile and allow an initial determination for G and λ for each PMT individually, then adjusting the PMT HV to produce a uniform overall response. Later, beam data taken with electrons can be used to estimate f_s and to cross-check the MIP calibration.

Initial PMT gain-matching was performed using cosmic-ray muons in a test setup prior to installation of each EC module in Hall B. For these tests, the EC modules were oriented horizontally so that muons, which have a zenith angle distribution proportional to $\cos^2\theta$, would enter mostly normal to the lead–scintillator sandwich. After installation in the hall, the vertical geometry was not as favorable for cosmic runs, so a special trigger and event filter was developed to single out the desired cosmic muon events.

Cosmic runs are performed using a special trigger that forces a hit in both the inner and outer stacks of the EC module. A software filter then accepts only events which activate a single pixel. A pixel is the smallest unit of x–y position resolution in the calorimeter, defined by the overlap of 3 scintillator stacks, one from each of the U, V and W views (Fig. 8). Requiring the muon to pass through both a single inner and outer pixel places the most restrictive cut possible on the particle track path length, thereby minimizing the spread in the energy deposition. Typically, cosmic runs require about 12 h to obtain 100 events/pixel.

The top panel of Fig. 10 shows a typical pulse height response of a single PMT to cosmic muon events subject to the pixel cut. This particular PMT is attached to a stack of long scintillators and the resulting MIP spectrum is broadened by the attenuation of light coming from different pixels within the stack. Since the scintillator strips vary in length from 10 to 470 cm, the mean and shape of the MIP distribution will depend on the stack.

The bottom panel of Fig. 10 shows the mean of the MIP distribution as a function of pixel distance from the PMT. The solid line is an exponential fit,

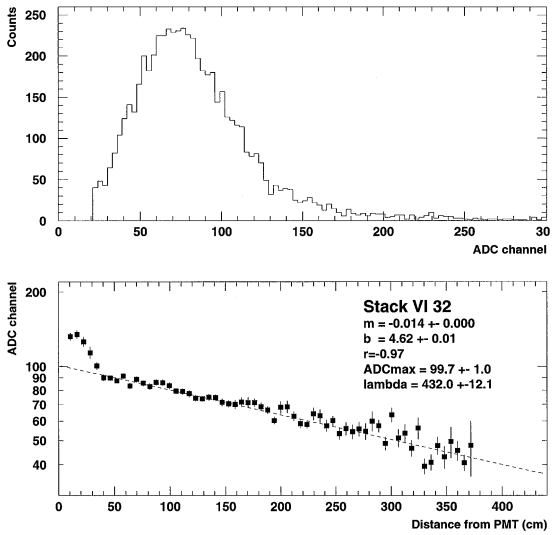

Fig. 10. Top: Pulse height distribution of energy deposited by cosmic muons in inner stack V32. Only events passing pixel cut are shown. Bottom: Dependence of mean pulse height on pixel distance from PMT. Results from an exponential fit are shown. ADC_{max} is the extrapolated PMT gain in ADC channels. Lambda is the effective attenuation length of the scintillator stack. Note the large enhancement for pixels close to PMT, due to Cherenkov light generated by muons passing through light guides (see text).

from which the effective attenuation length λ and the unattenuated PMT gain G can be extracted. A pixel-dependent correction to the track length arising from the projective geometry is applied before fitting. The fit excludes the 5 pixels closest to the PMT, for which a large enhancement is seen which deviates from the smooth exponential dependence. This enhancement is caused by Cherenkov light generated by muons passing through the acrylic light guides at the rear of the calorimeter (shown in Fig. 3). Because of this effect this method is unreliable for PMTs viewing short stacks, since most of the muon trajectories pass through the light guides.

Comparison of the in situ measurement of stack attenuation lengths extracted from the cosmic-ray fits to values expected from the measurements of individual scintillator strips made before installation is shown in Fig. 11. Here the points labeled 'database' are calculated by taking the average over the scintillators making up each stack (5 strips for

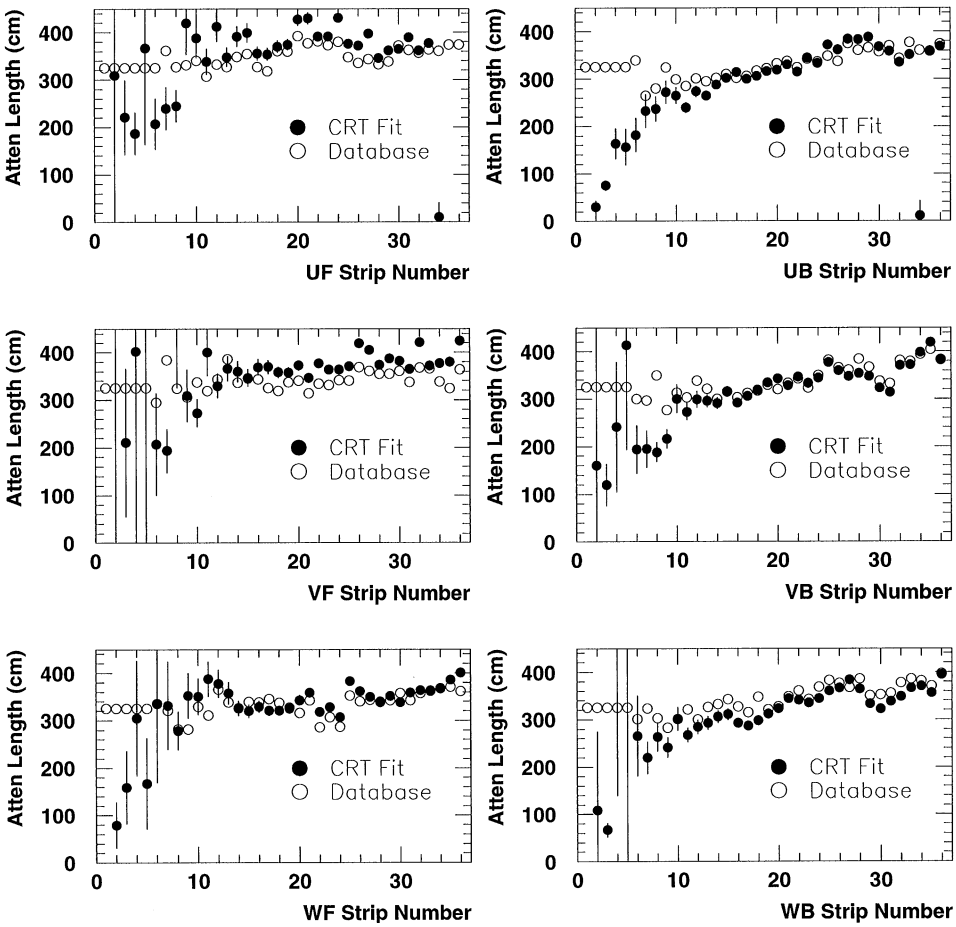

Fig. 11. Summary of stack-effective attenuation lengths extracted from fits to cosmic-ray distributions such as shown in Fig. 10, for all stacks in sector 3. Points labeled database are calculated from measurements of individual scintillator strips made before installation (see text).

inner stacks and 8 strips for outer stacks). Good agreement is seen, although some systematic shifts are evident. For short strips, the fits are biased by the light guide contributions just discussed and abnormally low attenuation lengths are extracted. For strips 1–8, the fitted results shown in Fig. 11 were not used to extract G and λ. Instead, attenuation lengths were calculated from the database and an event-weighted attenuation correction was applied to the mean pulse height to obtain G.

The desired ADC calibration was 10 channels/MeV, which would produce minimum ionizing distributions peaking at channel 100 (160) for inner (outer) stacks, assuming an MIP energy loss of 2 MeV/cm for scintillator. PMT high voltages were iteratively adjusted until the gains G resulting from the cosmic-ray fits matched (within 5%) the desired calibrations. These gains were then used for the initial round of data taking with an electron beam.

10. Preliminary performance

After a brief commissioning period in which rates and backgrounds were studied and optimum beam tunes were established, preliminary data-taking runs were begun in December 1997 using electron beam energies of 1.645, 2.445 and 4.045 GeV.

Future articles will provide details of the CLAS performance as a whole. Here we summarize the preliminary performance of the EC modules.

10.1. Electron response

The energy response of an EC module to electrons is shown in Fig. 12. Electron candidates were selected by demanding in software a match between the reconstructed position of a hit in the EC (discussed in the next section) and the extrapolated hit position of a negatively charged particle track identified by the Drift Chambers (DC). The left panel of Fig. 12 shows EC-reconstructed energy versus the momentum of the DC track. The strong correlation between measured energy and momentum shows that most of these events are electrons.

Pion events were largely suppressed by placing the EC total energy threshold E_{tot} in the hardware trigger at 0.6 GeV electron energy, which is about twice the minimum ionizing energy deposition. This threshold is evident in Fig. 12 by the strong decrease in event density at threshold. Events appearing below the threshold occur when a different

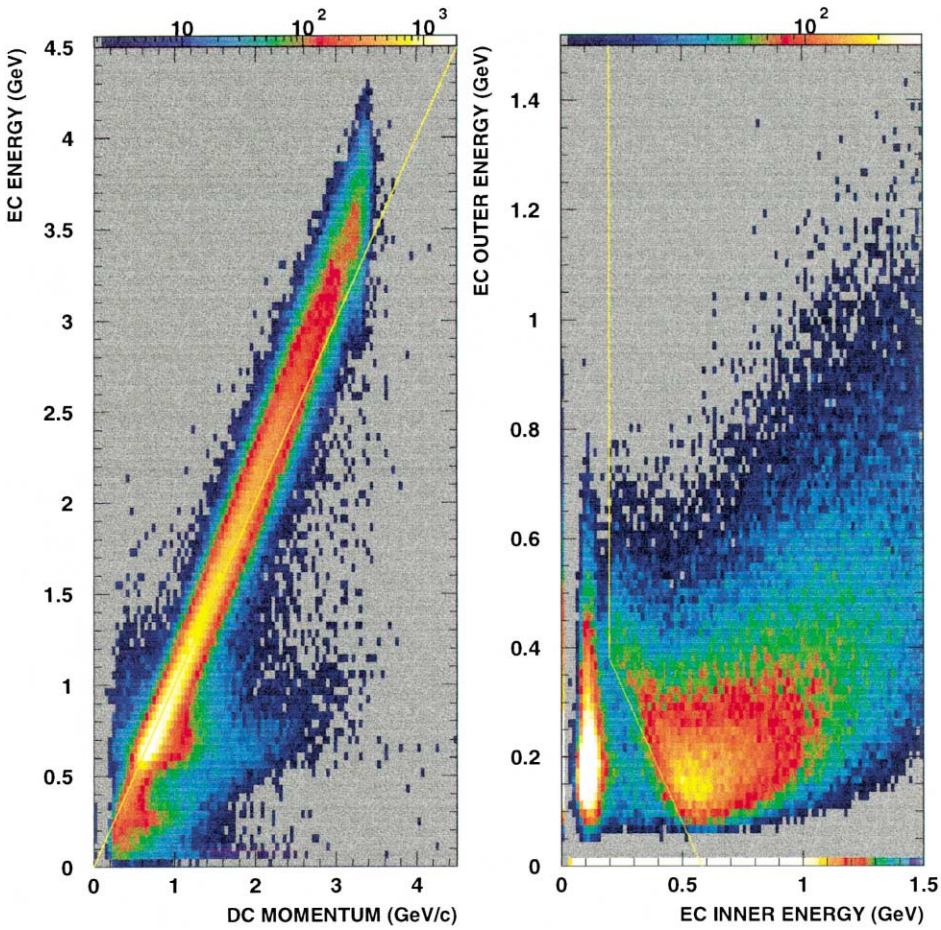

Fig. 12. Left: Energy of reconstructed hit in EC (y-axis) plotted versus momentum of matched negative track measured by Drift Chambers (x-axis). Hardware trigger threshold was set for 0.6 GeV. Events below threshold due to triggers from other sectors. Right: Reconstructed energy in outer EC stacks (y-axis) versus inner EC stacks (x-axis). Hardware trigger required a coincidence $EC_{inner} \cdot EC_{tot}$ using energy thresholds indicated by solid lines. Trigger rejected minimum-ionizing pions and hadronic interaction tail shown below threshold cuts.

sector produces the trigger or when the calorimeter which causes the trigger has more than one reconstructed hit. Further suppression of pions above the hardware threshold was provided by putting the Cherenkov Counter (CC) in the trigger and demanding in software a match between the EC hit and the appropriate segment of the CC. Residual pion contamination above threshold probably originated from $\pi^- p \rightarrow \pi^\circ n$ charge exchange inside the EC, followed by e^+, e^- backspash into the CC from π° initiated EM showers.

Separate readout of inner and outer EC stacks permits longitudinal sampling of the deposited energy. The right panel of Fig. 12 shows outer energy versus inner energy for the same sample of events shown at left. The diagonal line represents the trigger threshold of 0.6 GeV placed on the total energy $E_{tot} = E_{inner} + E_{outer}$. Above this threshold, the energy deposition is dominated by EM showers coming from electron triggers, which mostly deposit energy in the inner stacks. Below the threshold, pions are visible (correlated with electron triggers in the same or other sectors) as a sharp minimum-ionizing energy peak in the inner stack, with a long energy tail as measured by the outer stack. The tail is due to strong interactions within the calorimeter which produce forward going hadronic debris that smears the MIP peak in the outer stack.

These hadronic tails can exceed the E_{tot} threshold, but their suppression is possible by forming a coincidence trigger $E_{inner} \cdot E_{tot}$, with the additional requirement that the energy deposited in the EC inner stacks be just above the MIP peak seen in Fig. 12. This threshold is indicated by the vertical

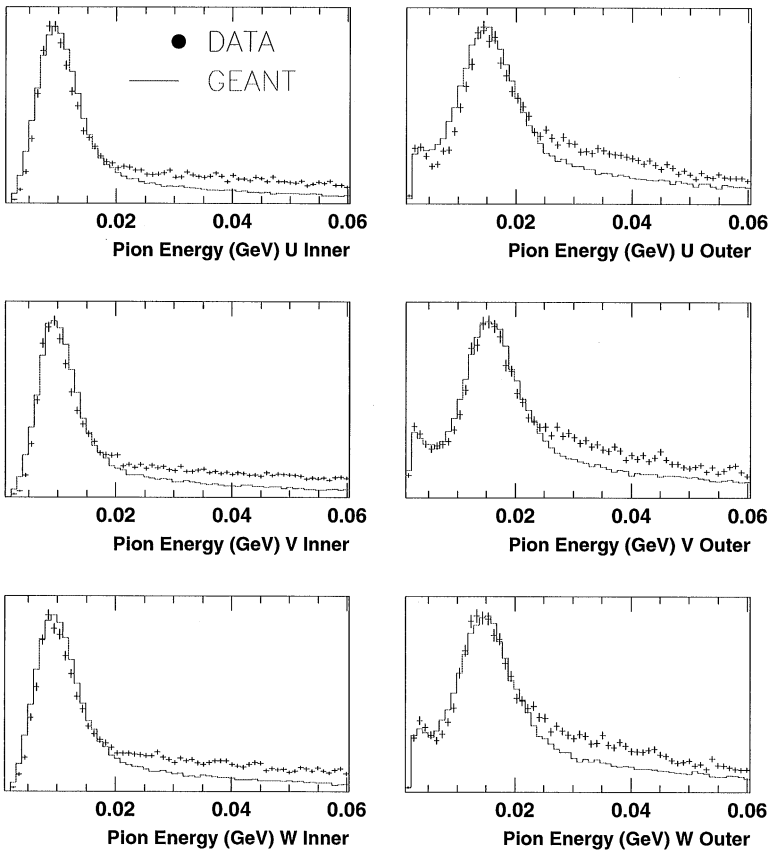

Fig. 13. Energy loss distribution of positive pions in EC. Data are compared to GEANT simulation (curve) for inner and outer stacks.

line and is seen to have minimal impact on the electrons.

The EC energy calibration in the MIP regime was checked by measuring the deposited energy left by MIP pions. Fig. 13 shows the average reconstructed energy for positive pions in each of the (U, V, W) stack views. Agreement at the 10% level with the GEANT simulation is seen for both peak position and width, indicating relative gain matching and absolute calibration provided by the cosmic muon MIP calibration is reliable to this order. However, hadronic tails tend to distort these distributions somewhat and a more detailed analysis will be necessary to allow extractions of G and λ for each PMT with the same level of accuracy as from cosmic muons.

The measured sampling fraction and energy resolution for electrons in the energy range 0.5–4.0 GeV are compared to GEANT simulations in Fig. 14. Here the sampling fraction f_s is defined as the ratio of the reconstructed energy E_{tot} to the momentum P determined from the drift chambers. It is seen that f_s has a stronger dependence on P than predicted by GEANT. Also, the overall magnitude of f_s is 5–13% higher than GEANT predictions, depending on which point on the GEANT curve is used for normalization. Energy resolution follows the expected $E^{-1/2}$ dependence, with an average resolution at 1 GeV of around 10–12%. This is somewhat larger than the $\approx 9\%$ predicted by GEANT, but is adequate for the purposes of setting the hardware trigger threshold [15]. These residual calibration errors show some systematic sector and position dependence at the 5–10% level, which may reflect uncertainties in our assumptions about the energy versus zenith angle distribution of cosmic muons, sector- or position-dependent variations in the thickness of lead and scintillator, or incorrect attenuation length corrections for the shorter strips. It is expected that these residual errors can eventually be calibrated out of the data.

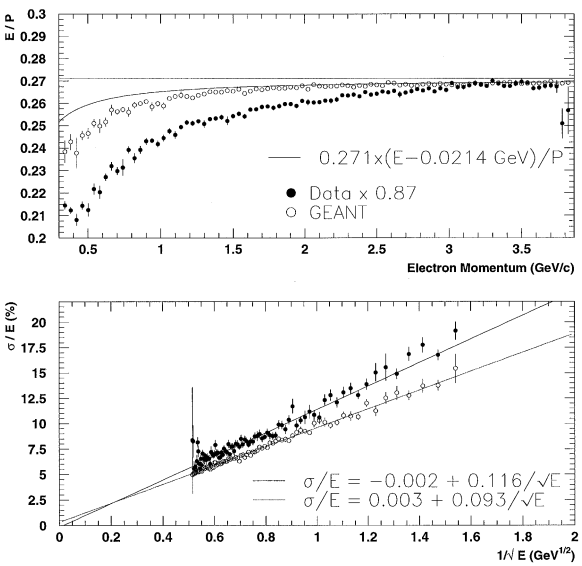

Fig. 14. Top: Measured sampling fraction $f_s = E/P$ for electrons. Data have been multiplied by a factor of 0.87 for comparison with GEANT. Bottom: Energy resolution σ/E for electrons over the same energy range. Straight line fits are shown for both GEANT and data.

10.2. Position resolution

One of the design requirements for CLAS was the ability to distinguish multiple hits within the same sector, as well as to discriminate between neutral and charged hits. The high degree of segmentation in the forward carriage detectors makes this possible, with the EC detectors having the finest granularity. Fig. 15 shows the event density of reconstructed EC electron hits as a function of the hit position in all six EC modules during a typical run. The spatial location of each reconstructed hit was determined from the EC stereo readout, where typically 8 scintillator strips were involved in an EM shower. The number of events/bin in Fig. 15 is logarithmically weighted according to the scale shown at the top of the figure. The strong forward angle scattering typical of EM interactions results in a nearly 1000-fold variation in event flux over the angular acceptance of the calorimeter system. At the beam energy shown here (4.045 GeV) the accepted electron scattering angle range was $\theta_e = 12$–$70°$. At these energies, electron trigger rates at the design luminosity of $10^{34}\,\mathrm{cm}^{-2}\,\mathrm{s}^{-1}$ were typically less than 200 Hz per sector.

The EC position resolution was estimated from the EC–DC track matching residuals. These are shown in Fig. 16 for both x and y directions in sector 1. Gaussian fits indicate an overall RMS

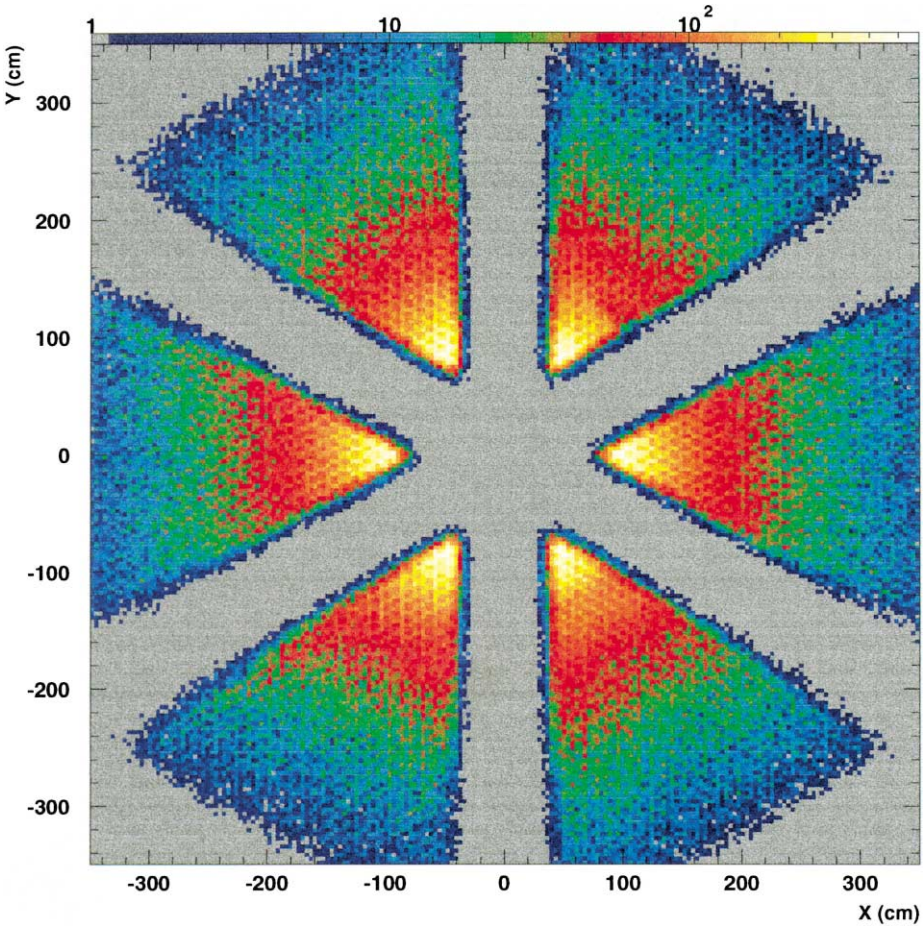

Fig. 15. Distribution of reconstructed electron hits across face of calorimeters in sectors 1–6. View is looking downstream along beam axis (located at $X = Y = 0.0$). Beam energy was 4.045 GeV. Event density in events/bin is logarithmically weighted according to the scale at top.

resolution $\sigma_{xy} \approx 2.3$ cm. For UVW stereo reconstruction using 10 cm wide strips $\sigma_{xy} \approx 10/\sqrt{12} = 2.9$ cm is expected. The non-Gaussian tails are two orders of magnitude below the peak and probably arise from fluctuations in the transverse profile of the EM shower which occur in the outer calorimeters (see Fig. 7). A summary of the track-matching residuals for all six sectors (bottom of Fig. 16) shows that the relative alignment of the EC modules and the drift chambers is within 2 cm, although some systematic shift is evident in the x-coordinate. These measured misalignments together with survey data are used to refine the reconstruction and simulation software.

10.3. Reconstruction of $\pi^\circ \to 2\gamma$ decays

Neutral hits in the EC were identified by the absence of a matched DC track. Candidate events corresponding to $\pi^\circ \to 2\gamma$ decays were required to have at least two neutral EC hits in any sector. Fig. 17 (top left) shows for such events the product of the neutral hit energies E_1E_2 versus the opening angle between the hits, calculated using the reconstructed hit position. The data show a clear band of $\pi^\circ \to 2\gamma$ decays occurring within the invariant mass range 0.1–0.2 GeV calculated using Eq. (1). The data were taken using a 0.5–2.4 GeV photon beam incident on an LH_2

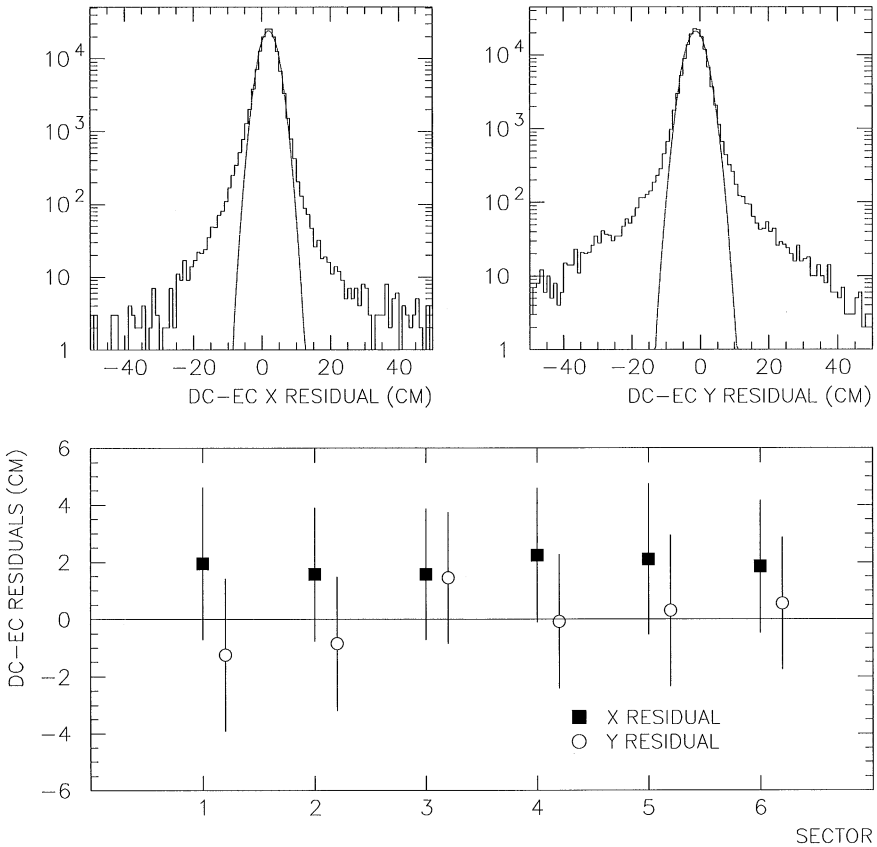

Fig. 16. Histograms show difference between reconstructed EC hit position and projected hit position of track reconstructed from drift chambers (DC) for sector 1. Results from Gaussian fits to all 6 sectors are shown in the graph at bottom, where the fitted means and standard deviations are plotted. Overall EC position resolution is $\sigma \approx 2.3$ cm.

target. No photon/neutron discrimination was performed.

Another check on the absolute EC energy calibration was provided by calculating the π° mass separately for each sector. For this check only events in which both decay photons hit the same EC module were analyzed, restricting the opening angle θ_{12} to be less than 25°. Fig. 17 (bottom left and right) shows that the overall calibration is within $\pm 5\%$ of the π° mass, with the resolution $\delta m/m \approx 0.11$–0.14, within the design specifications.

10.4. Neutron detection

The EC neutron detection efficiency was measured using the p(e, e′π^+)n reaction [16]. Neutrons were identified by the missing mass technique for events containing an identified electron and positive pion, and no other charged particles. A vertex cut removed any events due to the entrance and exit foils of the liquid hydrogen target. Only events with missing momentum pointing into the fiducial region of the EC were selected, to avoid edge effects. True neutron hits were identified by requiring the direction of the missing momentum to be the same as the direction of a measured neutral hit on the calorimeter within its angular resolution, assuming the target center as origin. Hits on all three views of the calorimeter were required (although only two are necessary for the hit position determination).

The result of this study is shown in Fig. 18. The efficiency rises from zero at 0.4 GeV/c to a plateau

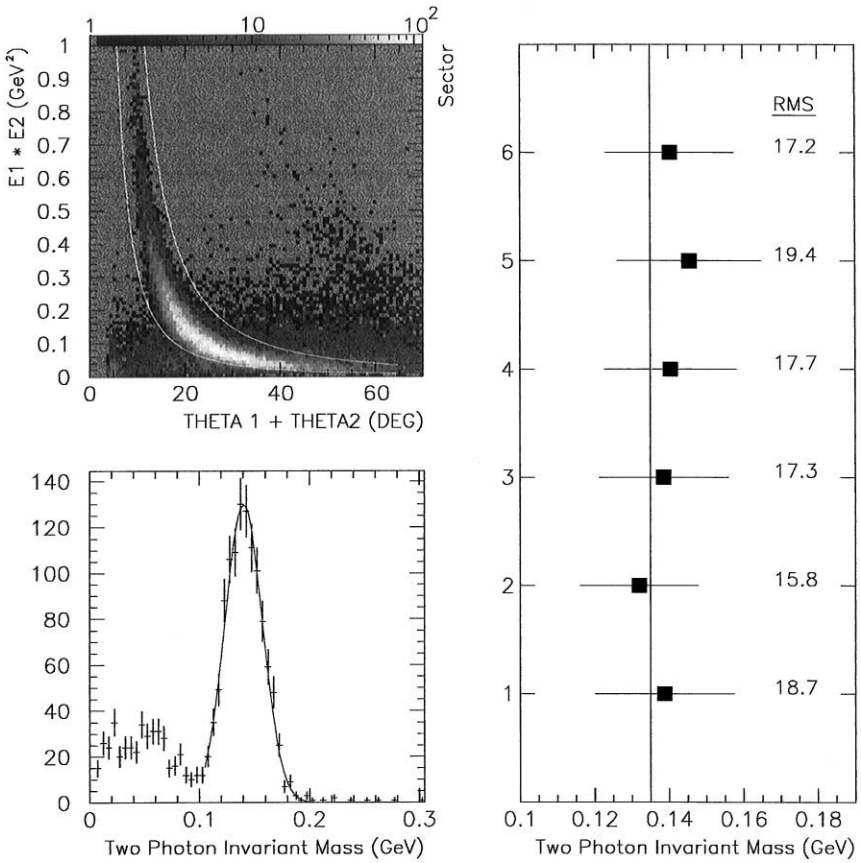

Fig. 17. Top left: Distribution of E_1E_2 versus opening angle of 2 neutral hits detected in EC. Curves show constant invariant mass ($M^2 = 2\,E_1E_2\,(1-\cos\theta_{12})$) for 2 photon decay of particles having masses 0.1 and 0.2 GeV. Bottom left: Gaussian fit to measured π° invariant mass. Right: Sector dependence of π° invariant mass where both photons are detected in the same sector. RMS resolution displayed as error bars and listed at right in units of MeV.

of approximately 60% above 1.6 GeV/c. This result is consistent both with expectations based on nuclear interaction lengths and more detailed GEANT simulations.

10.5. Timing calibration

There are several possible uses for good EC timing in CLAS. The essential ones are to discriminate between photons and neutrons, and to calculate neutron kinetic energy. In addition, in the case that any channels in the time-of-flight counters are inoperative in the forward region of the spectrometer, the EC timing resolution for charged particles is sufficient to provide a start time for the drift chambers and to identify the RF pulse corresponding to the beam electron initiating the event.

The timing calibration of the EC was performed using charged particles which passed through both the time-of-flight scintillators and the forward calorimeter. Electrons and charged pions were used simultaneously to span the full range of angles and deposited energy. Only events with a single charged track in a given sector were used. Using a large sample of data (1–2 M charged particle events), a chi-squared minimization was performed to compare the timing from the time-of-flight detectors to that of the EC using a five-parameter model for the EC time. The five parameters of the model included an additive constant, a tdc slope parameter, one

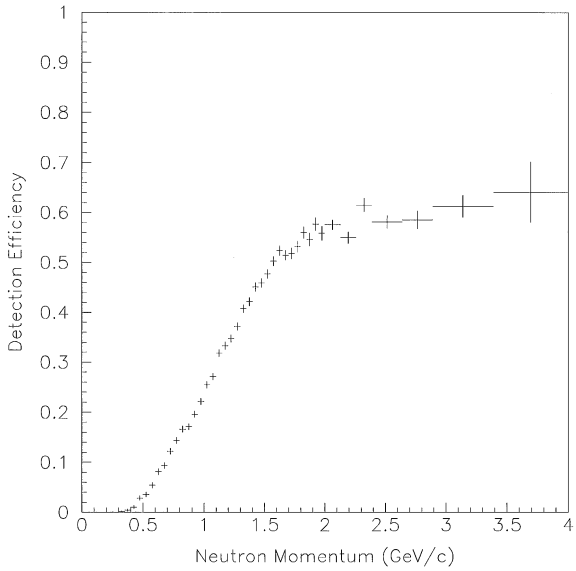

Fig. 18. Measured neutron detection efficiency in EC module. Reaction p(e, e′π⁺)n was used to tag neutrons entering calorimeter fiducial area.

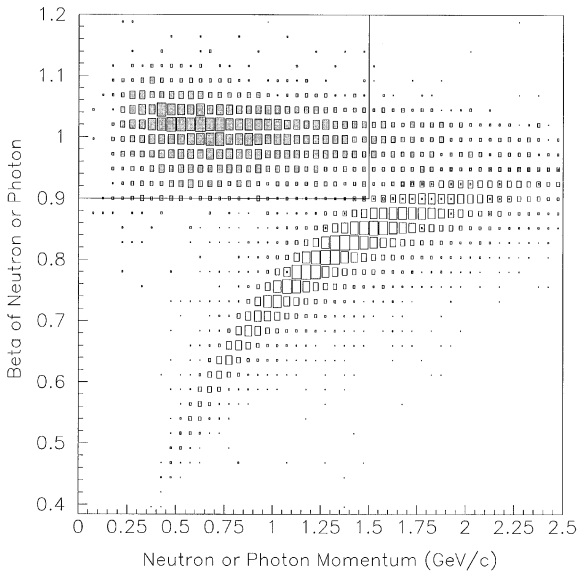

Fig. 19. Neutron/photon discrimination in the EC modules. The measured beta is plotted against momentum. Neutrons and photons were kinematically tagged and their momenta inferred either from kinematics (for neutrons) or deposited EC energy (for photons). Box refers to cut discussed in text.

walk correction parameter, and two parameters to take into account time slewing due to geometric effects. The signal propagation velocity was assumed to be constant. Although each calculation of the chi-squared involved a separate pass through all the data, the entire calibration procedure required only about 30 min for a given data set.

The timing accuracy achieved thus far for electrons of a few GeV is better than 200 ps; for the neutron and photon sample of this study, timing accuracies in the range 500–600 ps have been obtained. Further improvement is anticipated for both charged particles and neutrals.

Fig. 19 shows a comparison of photon timing to neutron timing in the EC. Neutrons were kinematically tagged using the $p(e, e'\pi^+)n$ reaction as previously described. Photons were tagged using the $p(e, e'\pi^+)\pi^\circ$ reaction. An electron and a proton were identified by the drift chambers and time-of-flight system, and a missing mass cut was placed around the π° peak. For some of these events both photons from the $\pi^\circ \to 2\gamma$ decay would strike the calorimeters. To identify these photons, a pion invariant mass was calculated from the measured angles and energy deposits for two neutral hits on the EC which satisfied the missing mass cut. A deposited energy of at least 5 MeV was required in both the inner and outer calorimeter modules to remove any remaining background neutrons. The resulting pure sample of photons can be seen to be easily distinguished from the neutrons with a β cut of 0.9 up to 1.5 GeV. At higher momenta, neutrons can be identified by excluding neutral hits in the inner module of the calorimeter. Although this reduces the neutron detection efficiency plateau to approximately 40%, it efficiently removes photons since they rarely pass through six radiation lengths without depositing detectable energy.

11. Conclusions

We have designed, built, tested and installed six EM calorimeter modules utilizing a novel geometry, segmentation and readout scheme, which are now functioning in their role of providing the high-energy forward angle trigger for CLAS. All six modules have met or are close to meeting their

design criteria for position, energy and timing resolution. Analysis of the initial round of data taking with CLAS is underway and is expected to allow us to refine our calibration procedures and optimize the detector response.

Acknowledgments

The authors wish to thank University of Virginia students Timothy Evans, Michael Ficenec, Justin Harrell, Alysia Johnson, Nathan McDannold, Nathan Nicely, John-Paul Shebalin and Penelope Slocum for their tireless effort in performing the measurements of several thousand scintillator strips. Thanks go to James Madison University students R. Atkins, D. Bailey, S. Bowling, A. Brotman, H. Dawson, T. Deering, P. Denholm, D. Ellis, J. Fennel, M. Fox, D. Gilmore, K. Healey, D. Hogue, J. Krug, A. Larson, J. Masters, D. McNulty, W. Opaska, A. Pastor, K. Tchikhatchev, Y. Tsganenko, W. Vogan, A. Volya and J. Voshell who helped design, build and install the laser calibration system and evaluate the PMTs. Help was also received from DongHee Kim, Chanhoon Chung, Wonha Ko, Minjeong Kim, Minsuk Kim and Sohn Young-Soo of Kyungpook National University and Troels Petersen of the Niels Bohr Institute. Thanks also go to the technicians at Jefferson Lab for their careful work in stacking the lead/scintillator layers of each EC module and installing the detectors in CLAS. This work was supported in part by DOE contract DEFG02-97ER41018 and NSF grants PHY-921507 and PHY-9600454.

References

[1] K. Beard, V. Burkert, R.A. Eisenstein, H.O. Funsten, M. Gai, K. Giovanetti, A.D. Hancock, K.J. Healey, D.W. Hertzog, D. Joyce, J.R. Kane, J. Lieb, W.F. Vulcan, Lead/scintillating fiber electromagnetic calorimeter prototype, CLAS-NOTE-90-013, 1990.

[2] R. Minehart, M. Amaryan, K. Beard, S.K. Bowling, V. Burkert, R. Demirchyan, Y. Efremenko, H.O. Funsten, K. Giovanetti, D. Joyce, L. Kramer, J. Lieb, R.M. Marshall, R. Sealock, L.C. Smith, P.K. Teng, S. Thornton, H. Weller, Lead–scintillator electromagnetic calorimeter with stereo readout, CLAS-NOTE-90-014, 1990.

[3] V. Burkert, Yu. Efremenko, K. Egiyan, K. Giovanetti, V. Gavrilov, H. Mkrtchan, E. Smith, S. Stepanyan, Photomultipliers for the electromagnetic shower calorimeter of the CEBAF large acceptance calorimeter, CLAS-NOTE-92-009, April 3, 1992.

[4] E. Smith et al., Nucl. Instr. and Meth. 432 (1999) 265.

[5] K.L. Giovanetti et al., Detailed report on the design and operation of the calibration system for the forward calorimeter for the CLAS detector, CLAS-NOTE-99-006, 1999.

[6] V. Burkert, P. Degtyarenko, E. Egiyan, S. Majewski, S. Marekhin, M. Ohanjanyan, Y. Sharabyan, R. Wojcik, Plastic scintillator and wavelength shifter tests for the CLAS electromagnetic calorimeter, CLAS-NOTE-91-005, March 6, 1991.

[7] V. Burkert, Y. Efremenko, K. Egiyan, S. Stepanyan, K. Giovanetti, Light readout system for the electromagnetic shower calorimeter of the CEBAF large acceptance spectrometer, CLAS-NOTE-92-008, March 31, 1992.

[8] R. Minehart et al., CEBAF PR-90-26, November 1990.

[9] K. Egiyan, Characteristics of scintillators and light readout system of CLAS forward electromagnetic calorimeter, CLAS-NOTE-99-009, 1999.

[10] Catalogue of Bicron Corporation, 12345 Kinsman Road, Newbery, OH 44065-9677, USA, 1990.

[11] C. Zorn et al., Fourth International Conference on Calorimetry in High Energy Physics, Italy, September 1993, World Scientific, Singapore, 1994.

[12] R. Demirchyan, GEANT simulation of CLAS forward calorimeter performance, CLAS-NOTE-93-009, August, 17, 1993.

[13] M. Guidal, GEANT simulation program for CLAS, CLAS-NOTE-93-013, 1993.

[14] K.B. Beard, Ec 3.1.2 forward electromagnetic calorimeter reconstruction software, CLAS-NOTE-93-012, 1993.

[15] K.S. Egiyan, Determination of electron energy cut due to the CLAS EC threshold, CLAS-NOTE-99-007, 1999.

[16] E. Hackett, W. Brooks, Neutron detection in the CLAS calorimeters: a first measurement, CLAS-NOTE-98-014, 1998.

[17] CEBAF Hall B Conceptual Design Report, April 1990.

[18] GEANT 3.2.1 CERN Program Library Long Writeup W5013.